ICCM2012
November 25-27, 2012, Gold Coast, Australia
www.ICCM-2012.org

Compact local Integrated RBF stencil based on Finite Volume formulation for second-order differential problems

T.-T Hoang-Trieu[1*], N. Mai-Duy[1], C-D. Tran[1], and T. Tran-Cong[1]
[1] *Computational Engineering and Science Research Centre, Faculty of Engineering and Surveying, University of Southern Queensland, Toowoomba, QLD 4350, Australia*
[*] *Corresponding author: thuy-tram.hoang-trieu@usq.edu.au*

Abstract

In this paper, compact local integrated radial basis function (RBF) stencils (Mai-Duy and Tran-Cong, 2011) are incorporated into the finite-volume formulation for the discretisation of second-order differential problems. The unknown field variable and its derivatives are approximated using compact integrated RBFs defined on local regions that cover the problem domain. The governing equation is integrated over non-overlapping control volumes associated with nodes, and the divergence theorem is then applied to convert volume integrals into line integrals. Line integrals are evaluated by the middle point rule. The proposed scheme is numerically verified through the solution of several test problems including natural convection flows. Numerical results indicate that the proposed method outperforms the standard finite volume method.

Keywords: Integrated RBF, Compact local IRBF approximations, Finite volume method, Thermal natural convection flows.

Introduction

Finite volume methods (FVMs), which conserve mass, momentum and energy over any control volume and can work effectively with complex geometry problems, have been widely used in computational fluid dynamic (CFD) (Patankar, 1980).

RBFs have been developed as a high order approximator for over twenty years. They can be classified into differentiated and integrated RBFs (DRBFs and IRBFs). The latter, in which the highest order derivatives are decomposed into a set of RBFs, and the lower-order derivatives and the function itself are then calculated by integration, has the ability to avoid the reduction of convergence rate caused by differentiation (Mai-Duy and Tran-Cong, 2003). In recent years, research effort has been focused on constructing IRBF approximations in local (to obtain sparse system matrices) and compact local (to obtain both sparse system matrices and high rates of convergence) forms (Mai-Duy and Tran-Cong, 2011).

Global and local IRBFs have been introduced into not only the point collocation formulation, which is meshless in nature, but also some other formulations, such as the Galerkin (Ho-Minh et al, 2009), moving least square (Ngo-Cong et al, 2012), and subregion collocation (Kansa et al, 2004). In this paper, we incorporate compact local IRBFs into the finite volume (subregion collocation) formulation to approximate the field variable and its derivatives, where the extra information about partial differential equations (PDEs) is included with the help of the integration constants and the middle point rule is utilised to evaluate line integrals. The proposed method is numerically verified

in some test problems governed by Poisson equation and the streamfunction-vorticity formulation. The remainder of the paper is organised as follows. The proposed method is presented in Section 2 and verified in Section 3. Section 4 concludes the paper.

Proposed method

Consider Poisson equation

$$\nabla^2 u(\mathbf{x}) = f(\mathbf{x}), \quad \mathbf{x} \in \Omega \tag{1}$$

where $\mathbf{x} = (x, y)^T$ is the position vector, Ω is the domain of interest and f is a forcing function.

Control volume discretisation

The problem domain is embedded in Cartesian grid $n_x \times n_y$. For each interior node (i, j) (i.e. (x_i, y_j), $2 \le i \le n_x - 1, 2 \le j \le n_y - 1$), we define its associated control volume as shown in Figure 1.

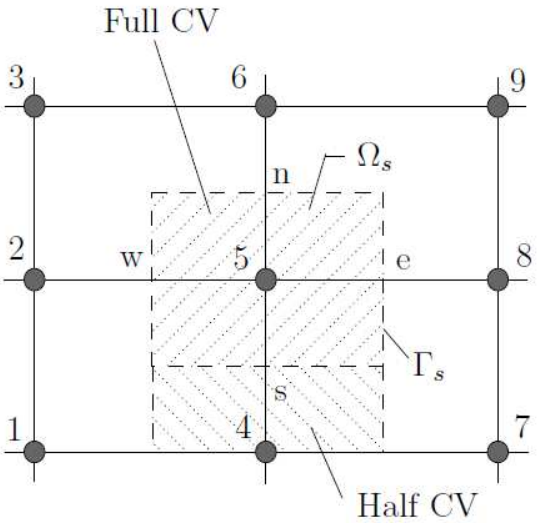

Figure 1. A schematic 9-node stencil

Integrating (1) over a control volume Ω_s results in

$$\int_{\Omega_s} \nabla^2 u d\Omega_s = \int_{\Omega_s} f(x, y) d\Omega_s. \tag{2}$$

The divergence theorem is then employed to convert the volume integral in the left side into surface integral

$$\int_{\Gamma_s} \nabla u \cdot \vec{n} d\Gamma_s = \int_{\Omega_s} f(x, y) d\Omega_s, \tag{3}$$

where $\vec{n}$ is the outward unit vector normal to the surface Γ_s. Making use of the middle point rule, equation (3) reduces to

$$\left[\left(\frac{\partial u}{\partial x}\right)_e - \left(\frac{\partial u}{\partial x}\right)_w\right]\Delta y + \left[\left(\frac{\partial u}{\partial y}\right)_n - \left(\frac{\partial u}{\partial y}\right)_s\right]\Delta x = \Delta x \Delta y f(x, y), \tag{4}$$

where the subscripts e, w, n and s are used to indicate the intersections of the grid lines with the east, west, north and south faces of the control volume, respectively; $\Delta x = x_e - x_w$ and $\Delta y = y_n - y_s$. In the case of Dirichlet boundary condition, no special treatment is required. In the case of Neumann boundary condition, the field variable is not given and one thus has to define one more equation, which can be based on the given Neumann boundary condition and a half control volume, to obtain that unknown.

Compact local IRBF approximation

Consider a 9-node stencil identified by the central node (i, j). Assume that the stencil is locally numbered from left to right and from bottom to top (Figure 1) ($(i, j) \equiv$ node 5). Hereafter, for brevity, we will use $\mathbf{x_k} = (x_k, y_k)$ to represent a grid node k in a local 2D stencil. For the x direction, the second derivative of function u is first decomposed into RBFs

$$\frac{\partial^2 u(\mathbf{x})}{\partial x^2} = \sum_{i=1}^{9} w_i^{[x]} I_{[x]i}^{(2)}(\mathbf{x}), \tag{5}$$

where $\left\{w_i^{[x]}\right\}_{i=1}^{9}$ is the set of weights; and $\left\{I_{[x]i}^{(2)}(\mathbf{x})\right\}_{i=1}^{9}$ is the set of RBFs, which are chosen as Multiquadric functions (MQ) in this study. The first derivative and the function itself are then obtained through integration

$$\frac{\partial u(\mathbf{x})}{\partial x} = \sum_{i=1}^{9} w_i^{[x]} I_{[x]i}^{(1)}(\mathbf{x}) + C_1^{[x]}(y), \tag{6}$$

$$u(\mathbf{x}) = \sum_{i=1}^{9} w_i^{[x]} I_{[x]i}^{(0)}(\mathbf{x}) + x C_1^{[x]}(y) + C_2^{[x]}(y), \tag{7}$$

where $I_{[x]i}^{(1)}(\mathbf{x}) = \int I_{[x]i}^{(2)}(\mathbf{x}) dx$; $I_{[x]i}^{(0)}(\mathbf{x}) = \int I_{[x]i}^{(1)}(\mathbf{x}) dx$; and $C_1^{[x]}(y)$ and $C_2^{[x]}(y)$ are the integration constants, which are functions of the variable *y*. In (5)-(7), the superscript (.) and notation [*x*] are used to denote the associated derivative order and quantity with respect to the x direction, respectively.

For the y direction, in the same way, one has

$$\frac{\partial^2 u(\mathbf{x})}{\partial y^2} = \sum_{i=1}^{9} w_i^{[y]} I_{[y]i}^{(2)}(\mathbf{x}), \tag{8}$$

$$\frac{\partial u(\mathbf{x})}{\partial y} = \sum_{i=1}^{9} w_i^{[y]} I_{[y]i}^{(1)}(\mathbf{x}) + C_1^{[y]}(x), \tag{9}$$

$$u(\mathbf{x}) = \sum_{i=1}^{9} w_i^{[y]} I_{[y]i}^{(0)}(\mathbf{x}) + y C_1^{[y]}(x) + C_2^{[y]}(x). \tag{10}$$

In this paper, the integration constants are also represented using IRBFs, which are based on a local grid $[\mathbf{x_1}, \mathbf{x_2}, \mathbf{x_3}]$ for approximation of $C_1^{[x]}(y)$ and $C_2^{[x]}(y)$, and $[\mathbf{x_1}, \mathbf{x_4}, \mathbf{x_7}]$ for approximation of $C_1^{[y]}(x)$ and $C_2^{[y]}(x)$.

The conversion matrix is obtained by collocating (5)-(7) and (8)-(10) at every grid point of the stencil

$$\begin{pmatrix} \hat{u} \\ \hat{0} \\ \hat{e} \end{pmatrix} = \underbrace{\begin{bmatrix} \mathcal{H}_x^{(0)} & \mathcal{O} \\ \mathcal{H}_x^{(0)} & -\mathcal{H}_y^{(0)} \\ \mathcal{K}_x & \mathcal{K}_y \end{bmatrix}}_{\hat{\mathcal{C}}} \begin{pmatrix} \widehat{w_x} \\ \widehat{w_y} \end{pmatrix} \tag{11}$$

where $\hat{0}$ and $\mathcal{O}$ are a vector and a matrix of zeros, respectively; $\hat{u}$ and $\hat{0}$ are vectors of length 9; $\widehat{w_x}$ and $\widehat{w_y}$ are the RBF coefficient vectors of length 15; $\mathcal{O}$, $\mathcal{H}_x^{(0)}$, $\mathcal{H}_y^{(0)}$ are matrices of dimensions 9×15; $\mathcal{K}_x$ and $\mathcal{K}_y$ are matrices of dimensions 4×15; equations $\hat{u} = \mathcal{H}_x^{(0)}\widehat{w_x}$ are employed to collocate the variable u over the stencil; equations $\mathcal{H}_x^{(0)}\widehat{w_x} - \mathcal{H}_y^{(0)}\widehat{w_y} = 0$ are employed to enforce nodal values of u obtained from the integration with respect to x and y to be identical; and equations $\mathcal{K}_x\widehat{w_x} + \mathcal{K}_y\widehat{w_x} = \hat{e}$ are employed to represent values of the PDE (1) at selected nodes $(\mathbf{x}_2, \mathbf{x}_4, \mathbf{x}_6, \mathbf{x}_8)$. Further details can be found in (Mai-Duy and Tran-Cong, 2011).

Solving (11) yields

$$\begin{pmatrix} \widehat{w_x} \\ \widehat{w_y} \end{pmatrix} = \mathcal{C}^{-1} \begin{pmatrix} \hat{u} \\ \hat{0} \\ \hat{e} \end{pmatrix} \tag{12}$$

or $\widehat{w_x} = \mathcal{C}_x^{-1}(\hat{u}, \quad \hat{0}, \quad \hat{e})^T$ and $\widehat{w_y} = \mathcal{C}_y^{-1}(\hat{u}, \quad \hat{0}, \quad \hat{e})^T$, where $\mathcal{C}_x^{-1}$ and $\mathcal{C}_y^{-1}$ are the first and the last 15 rows of matrix $\mathcal{C}^{-1}$. One can thus calculate values of the first derivatives at an arbitrary point on the stencil in the physical space as

$$\frac{\partial u(\mathbf{x})}{\partial y} = \mathcal{H}_y^{(1)}\mathcal{C}_y^{-1}(\hat{u} \quad \hat{0} \quad \hat{e})^T, \tag{13}$$

$$\frac{\partial u(\mathbf{x})}{\partial y} = \mathcal{H}_y^{(1)}\mathcal{C}_y^{-1}(\hat{u} \quad \hat{0} \quad \hat{e})^T. \tag{14}$$

We employ (13) and (14) to estimate the fluxes in the FV equations, e.g. (4) in the x direction.

Numerical results

The solution accuracy is measured using the relative discrete L_2 norm

$$Ne(u) = \frac{\sqrt{\sum_{i=1}^{n}(u_i - u_i^e)^2}}{\sqrt{\sum_{i=1}^{n}(u_i^e)^2}} \tag{15}$$

where n is the number of collocation nodes, and u_i and u_i^e are the computed and exact solutions, respectively.

Example 1
The present method is first verified with

$$\frac{\partial^2 u}{\partial x^2}+\frac{\partial^2 u}{\partial y^2}=4(1-\pi^2)\sin(2\pi x)\sinh(2y)+16(1-\pi^2)\cosh(4x)\cos(4\pi y) \qquad (16)$$

where $-0.5\le x, y\le 0.5$. Its exact solution is $u^e(x,y)=\sin(2\pi x)\sinh(2y)+\cosh(4x)\cos(4\pi y)$. The calculation is performed with several grid densities 5×5,7×7,…,71×71. We consider 2 types of boundary conditions: (i) Dirichlet boundary condition only, and (ii) Dirichlet and Neumann boundary conditions. For the latter, Dirichlet boundary conditions are prescribed on $x=-0.5$ and $x=0.5$ with $-0.5\le y\le 0.5$, while Neumann boundary conditions are specified on $y=-0.5$ and $y=0.5$ with $-0.5\le x\le 0.5$.
Figures 2 and 3 display the solution accuracy and matrix condition number in the case of Dirichlet and of Dirichlet-Neumann boundary conditions, respectively. Results obtained by the standard FVM and local-IRBF FVM are also included for comparison purposes. For both types of boundary conditions, compact local IRBF FVM yield similar matrix condition but much better accuracy than local-IRBF FVM and standard FVM.

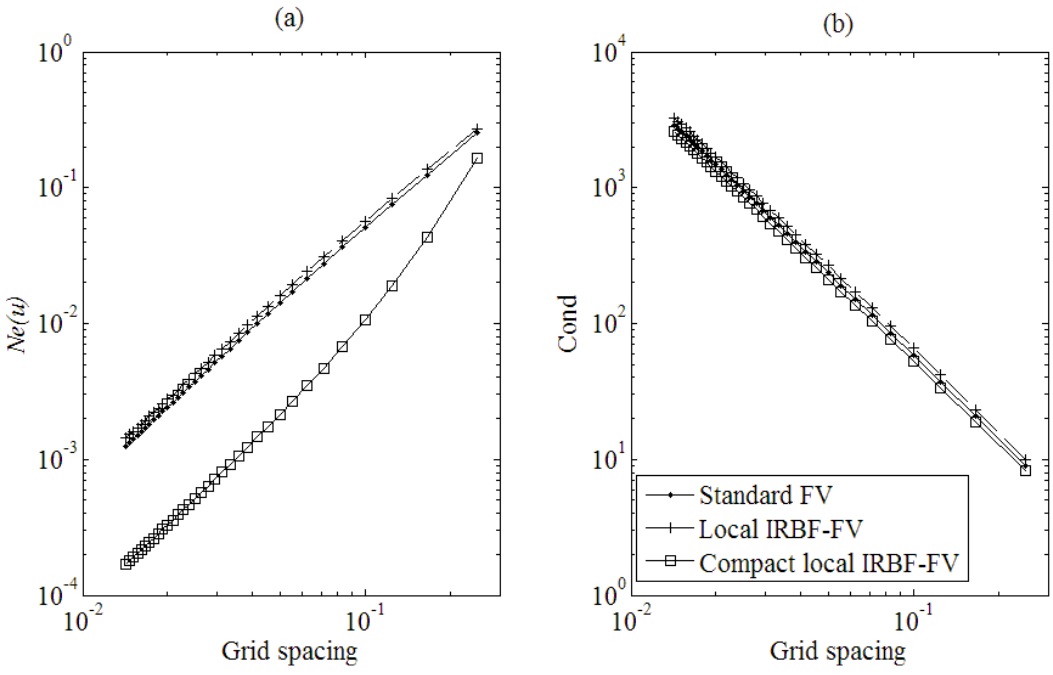

Figure 2. Example 1, Dirichlet boundary condition: Relative L_2 errors of the solution u and condition numbers of the system matrix against the grid size by local-IRBF FVM, standard FVM, and compact-local-IRBF FVM. The rates $O(Ne(u))$ are 1.86, 1.87, and 2.25, while $O(Cond)$ are 2.01, 2.01, and 2.00 by local-IRBF FVM, FVM, and compact-local-IRBF FVM, respectively.

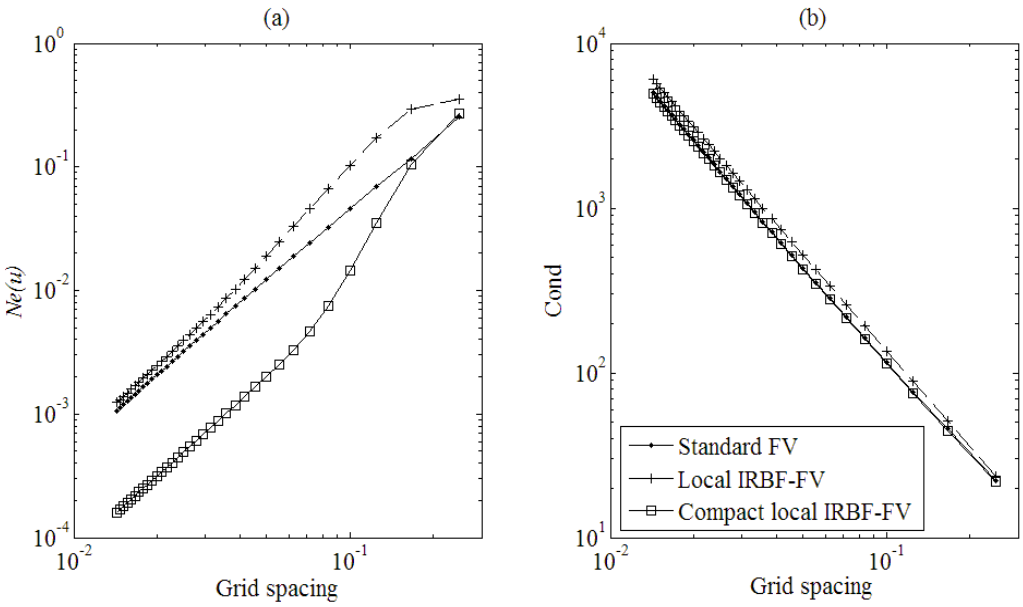

Figure 3. Example 1, Dirichlet and Neumann boundary conditions: Relative L_2 errors of the solution u and condition numbers of the system matrix against the grid size by local-IRBF FVM, standard FVM, and compact-local-IRBF FVM. The rates $O(Ne(u))$ are 2.18, 1.92 and 2.47, while $O(Cond)$ are 1.94, 1.92, and 1.92 by local-IRBF FVM, standard FVM, and compact-local-IRBF FVM, respectively.

Thermally Driven Cavity Flow Problem

The thermally driven square cavity flow (Figure 4) is one of several benchmark test problems, which is widely used to verify new numerical schemes.

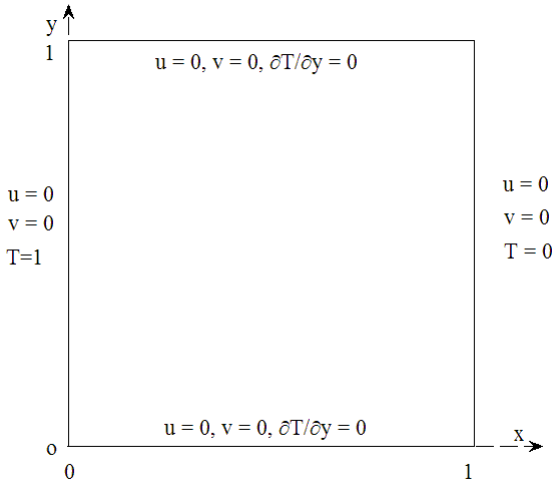

Figure 4. A schematic natural convection flow in a square slot. The problem is described in a stationary non-dimensional unit square ($0 \le x, y \le 1$). The two vertical walls are heated with temperature $T=1$ and $T=0$, while the horizontal walls are insulated.

The dimensionless governing equations can be written in terms of streamfunction ψ, vorticity ω, and temperature T as

$$\frac{\partial T}{\partial t}+\sqrt{RaPr}\left(\frac{\partial (uT)}{\partial x}+\frac{\partial (vT)}{\partial y}\right)=\frac{\partial^2 T}{\partial x^2}+\frac{\partial^2 T}{\partial y^2}, \tag{17}$$

$$-\omega=\frac{\partial^2 \psi}{\partial x^2}+\frac{\partial^2 \psi}{\partial y^2}, \tag{18}$$

$$\frac{\partial \omega}{\partial t}+\sqrt{\frac{Ra}{Pr}}\left(\frac{\partial (u\omega)}{\partial x}+\frac{\partial (v\omega)}{\partial y}-\frac{\partial T}{\partial x}\right)=\frac{\partial^2 \omega}{\partial x^2}+\frac{\partial^2 \omega}{\partial y^2}, \tag{19}$$

where $u=\frac{\partial \psi}{\partial y}$ and $v=-\frac{\partial \psi}{\partial x}$, Ra is the Rayleigh number, and $Pr = 0.71$ is the Prandtl number. The cavity is stationary, leading to $\psi = 0$ and $\partial\psi/\partial n = 0$ on the boundaries. We solve (18) with the boundary conditions $\psi = 0$. The vorticity on the walls, which is used to solve (19), is computed as $\omega = -\partial^2\psi/\partial n^2$, where $\partial\psi/\partial n = 0$ is included in $\partial^2\psi/\partial n^2$. One needs to integrate (17)-(19) over a control volume Ω_s. We assume that T and ω are constant over the control volume Ω_s and linear over the time interval $(t^{(k-1)}, t^{(k)})$, where the superscript (k) is used to indicate the current iteration. The time derivative term reduce to

$$\frac{\partial}{\partial t}\int_{\Omega_s}\mathbf{G}d\Omega_s=\frac{A}{\Delta t}\left(\mathbf{G}^{(k)}-\mathbf{G}^{(k-1)}\right), \tag{20}$$

where $\mathbf{G}$ represents quantities T and ω; A is the area of Ω_s.

The procedure involves the following steps

1. Solve (18) for ψ subject to Dirichlet conditions;
2. Compute the velocity components u and v and the boundary values for ω;
3. Solve (17) for T subject to Dirichlet and Neumann conditions;
4. Solve (19) for ω subject to Dirichlet conditions;
5. Repeat the above steps until the solution has reached the steady state.

Some important measures associated with this type of flow are

- Maximum horizontal velocity u_{max} on the vertical mid-plane and its location
- Maximum vertical velocity v_{max} on the horizontal mid-plane and its location
- The average Nusselt number throughout the cavity, which is defined as

$$\overline{Nu}=\int_0^1 Nu(x)dx, \tag{21}$$

$$Nu(x)=\int_0^1\left(uT-\frac{\partial T}{\partial x}\right)dy. \tag{22}$$

- The average Nusselt numbers on the vertical plane at $x = 0$ (left wall) and at $x = 1/2$ (middle cross-section), which are defined by

$$Nu_0 = Nu(x = 0, y), \tag{23}$$

$$Nu_{1/2} = Nu(x = 1/2, y). \tag{24}$$

A wide range of *Ra*, $(10^3,10^4,\ldots,10^7)$, is considered. The computed solution at the lower and nearest value of Ra is taken as the initial solution, and for the $Ra = 10^3$, the fluid is started from rest. The obtained results are compared with the benchmark solutions, which are reported by G. De Vahl Davis (1983) for $10^3 \le Ra \le 10^6$, and by P. Le Quere (1991) for $Ra \ge 10^6$.
Table 1 presents results obtained by the proposed method and other methods for several values of Ra. It can be seen that the present solutions are in better agreement with the benchmark ones than those obtained by the Galerkin-RBF approach reported in (Ho-Minh, 2009). Figure 5 displays the distribution of the streamfunction, vorticity and temperature over the flow domain. They look feasible in comparison with those reported in the literature.

Table 1: Natural convection flow in a square slot: Numerical solutions by compact-local-IRBF FVM and some other methods. It is noted that the solutions by Galerkin-RBF are taken at the highest densities used.

Ra	Density	u_{max}	*x*	v_{max}	*y*	$\overline{Nu}$	$Nu_{1/2}$	Nu_0
10^3	11×11	3.678	0.815	3.725	0.178	1.115	1.117	1.110
	21×21	3.650	0.813	3.698	0.179	1.117	1.118	1.116
	Galerkin-RBF[(a)]	-	-	-	-	1.118	1.119	1.117
	FDM[(b)]	3.649	0.813	3.697	0.178	1.118	1.118	1.117
10^4	11×11	16.454	0.822	19.865	0.128	2.279	2.275	2.276
	21×21	16.208	0.823	19.759	0.117	2.253	2.252	2.236
	31×31	16.191	0.823	19.682	0.119	2.248	2.248	2.242
	41×41	16.191	0.823	19.663	0.119	2.247	2.246	2.246
	Galerkin-RBF	-	-	-	-	2.247	2.248	2.244
	FDM	16.178	0.823	19.617	0.119	2.243	2.243	2.238
10^5	31×31	34.89	0.855	69.93	0.065	4.552	4.547	4.525
	41×41	34.72	0.855	69.06	0.065	4.528	4.524	4.514
	51×51	34.67	0.855	68.94	0.066	4.520	4.516	4.520
	Galerkin-RBF	-	-	-	-	4.529	4.530	4.521
	FDM	34.73	0.855	68.59	0.066	4.519	4.519	4.509
10^6	41×41	64.08	0.8521	225.63	0.0383	8.842	8.816	9.119
	51×51	64.60	0.8497	225.18	0.0375	8.876	8.856	8.892
	61×61	64.68	0.8501	223.25	0.0373	8.864	8.855	8.852
	71×71	64.46	0.8496	222.07	0.0376	8.829	8.809	8.825
	Galerkin-RBF	-	-	-	-	8.864	8.865	8.827
	FDM	64.63	0.8507	219.36	0.0379	8.800	8.799	8.817
	Spectral method[(c)]	64.83	0.850	220.6	0.038	8.825	8.825	-
10^7	71×71	141.251	0.887	713.098	0.022	16.486	16.410	18.005
	Galerkin-RBF	-	-	-	-	16.661	16.661	-
	Spectral method	148.595	0.879	699.179	0.021	16.523	16.523	-

[(a)] [Ho-Minh et al. 2009]
[(b)] [Davis, 1983]
[(c)] [Quere, 1991]

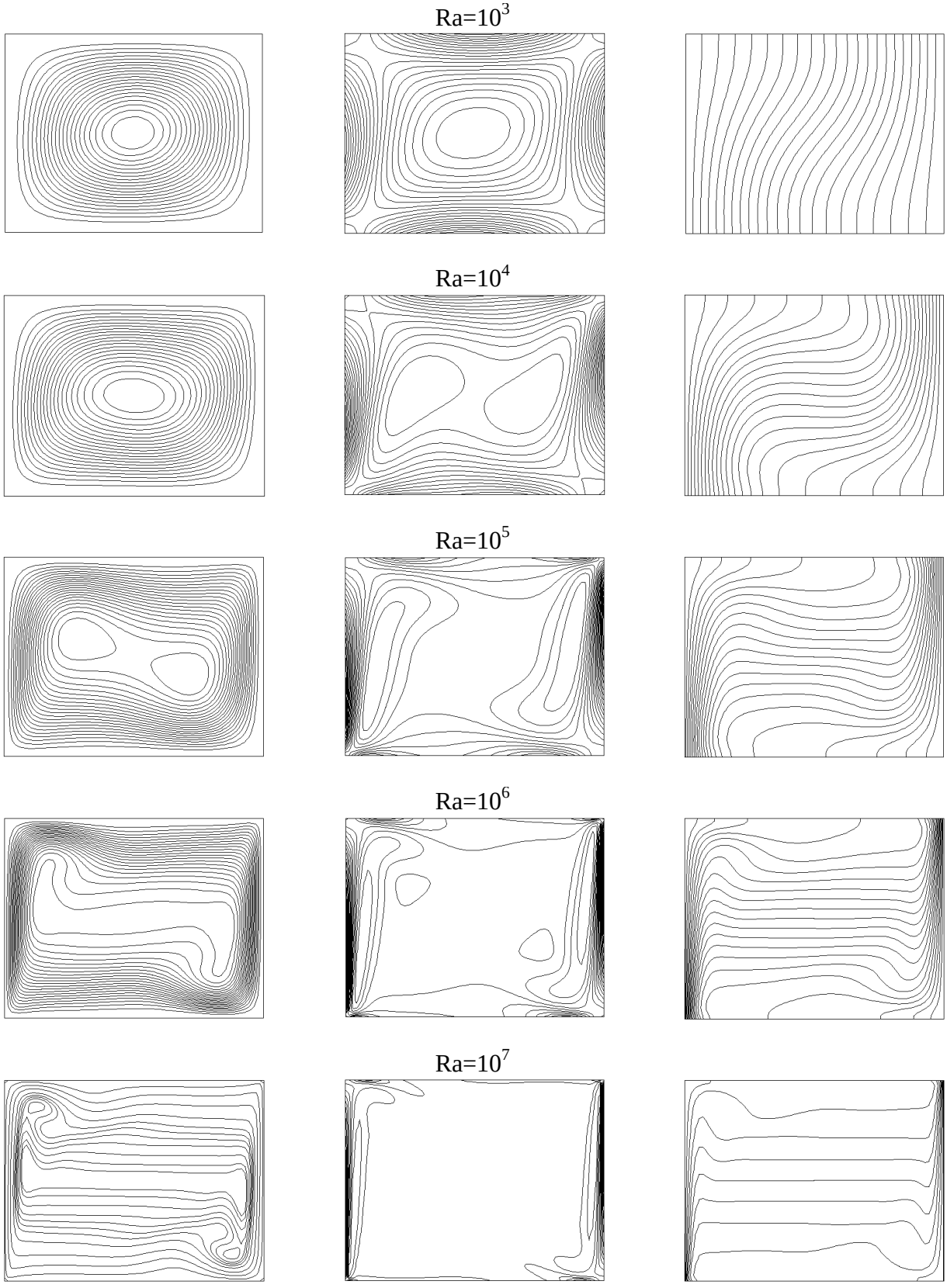

Figure 5. Natural convection flow in a square slot, grid of 71×71: Contour plots for streamline (left), vorticity (middle), and temperature (right).

Concluding remarks

This paper reports a new discretisation procedure, based on compact local IRBF stencils and subregion collocation, for heat transfer and fluid flow problems. The present technique is successfully verified in solving Poisson equation and natural convection flow. For Poisson equation, the method is superior to the standard FVM regarding both the accuracy and rate of convergence. For natural convection flow, a convergent solution is obtained at high values of the Rayleigh number and they are in good agreement with the benchmark solutions. However, the use of the middle point rule restricts the achievement of a high rate of convergence. Evaluating line integrals with a high-order Gauss quadrature rule is currently studied and the obtained results will be reported in future work.

Acknowledgement The first author would like to thank CESRC, FoES and USQ for a PhD scholarship. This research was supported by the Australian Research Council.

References

N. Mai-Duy and T. Tran-Cong (2011), Compact local integrated-RBF approximations for second-order elliptic differential problems. *Journal of Computational Physics*, 230, pp. 4772–4794.

S.V. Patankar (1980), *Numerical Heat Transfer and Fluid Flow*. McGraw-Hill, New York.

N. Mai-Duy and T. Tran-Cong (2003), Approximation of function and its derivatives using radial basis function networks. *Applied mathematical modeling*, 27, pp.197–220.

D. Ho-Minh, N. Mai-Duy, and T. Tran-Cong (2009), A Galerkin-RBF approach for the streamfunction-vorticity-temperature formulation of natural convection in 2D enclosured domains. *Computer Modeling in Engineering & Sciences*, 44, pp. 219–248.

D. Ngo-Cong, N. Mai-Duy, W. Karunasena, and T. Tran-Cong (2012), A numerical procedure based on 1D-IRBFN and local MLS-1D-IRBFN methods for fluid-structure interaction analysis. *Computer Modeling in Engineering & Sciences*, 83, pp. 459–498.

E.J. Kansa, H. Power, G.E. Fasshauer, and L. Ling (2004), A volumetric integral radial basis function method for time-dependent partial differential equations: I. Formulation. *Engineering Analysis with Boundary Elements*, 28, pp. 1191–1206.

G.D.V Davis (1983), Natural convection of air in a square cavity: a benchmark numerical solution. *International Journal for Numerical Methods in Fluids*, 3, pp. 249–264.

P.L. Quere (1991), Accurate solutions to the square thermally driven cavity at high Rayleigh number. *Computers Fluids*, 20, pp. 29–41.